

# Unusual Strain Dependence of Quasiparticle Electronic Structure, Exciton, and Optical Properties in Blue Phosphorene

Ju Zhou<sup>1</sup>, Tian-Yi Cai,<sup>1,\*</sup> and Sheng Ju<sup>1,2,3,†</sup>

<sup>1</sup>*Department of Physics and Jiangsu Key Laboratory of Thin Films, Soochow University, Suzhou 215006, P. R. China*

<sup>2</sup>*Department of Physics, University of California at Berkeley, California 94720, USA*

<sup>3</sup>*Materials Sciences Division, Lawrence Berkeley National Laboratory, Berkeley, California 94720, USA*

(Received 18 August 2020; revised 26 January 2021; accepted 27 January 2021; published 18 February 2021)

By considering many-body effects explicitly, we study the quasiparticle electronic structure, exciton, and optical properties of two-dimensional (2D) material blue phosphorene and their evolution with biaxial strain. Although the pristine system is an indirect wide-band-gap semiconductor, it could evolve systematically toward an almost direct one when an intermediate tensile strain is applied. The absorption edge shows an obvious red shift with an increase in the lattice constant, enabling its access to a wide spectral range. Interestingly, when the band gap increases, the exciton binding energy decreases. This unusual relationship is found to be accompanied by an enhanced exciton effective mass and decreased dielectric screening with an increase in the lattice constant. Together with the evolution of the band edge, a funnel effect is revealed in the inhomogeneously strained 2D membrane of blue phosphorene. The gate-controlled carriers at the two sides could drift efficiently toward the center with maximum strain, where the relatively strong binding energy and short lifetime are beneficial for the realization of the emission of green and blue light.

DOI: 10.1103/PhysRevApplied.15.024045

## I. INTRODUCTION

Since the discovery of graphene [1,2], two-dimensional (2D) materials have attracted wide interest in condensed-matter physics, materials science, and chemistry [3,4]. The unique layered crystal structure and the diversity of the electronic and optical properties have provided a useful platform to realize applications in electronics, photonics, and optoelectronics [5–10]. Despite being atomically thin, most 2D materials interact strongly with light due to a strong bound-exciton effect. As shown in Fig. 1, out of the optical band gaps of some representative systems, 2D materials could cover a wide spectral range. Graphene is a zero-band-gap semimetal and it interacts with light from microwave to ultraviolet wavelengths, thus making it useful in light detection, modulation, and manipulation over a wide range of spectra. However, its semimetallic nature prohibits the realization of efficient light-emitting devices, photovoltaic devices, and other optoelectronic devices. Black phosphorene (BP) and monolayers of transition-metal dichalcogenides (TMDs) are direct-band-gap semiconductors and the strong visible light absorption therein makes them very useful in

photovoltaics [11]. For the wide-band-gap semiconductors, except for the complicated Hittorf's phosphorene with its direct band gap (optical) at 2.4 eV [12–14], most of them are indirect-band-gap semiconductors, including blue phosphorene [15–20], III–VI monochalcogenide monolayers [21–24], and a boron nitride (BN) monolayer [25–27]. The indirect band gap greatly inhibits their immediate application as highly efficient light-emitting diodes (LEDs) for green, blue, violet, and even ultraviolet light [28].

Blue phosphorene, originally proposed by Zhu and Tománek [15], has been realized recently with the assistance of bottom-up growth techniques on metallic substrates [29–34]. Tellurium-monolayer-supported Au(111) has been used to reduce the interaction between the phosphorus and the metallic substrate and consequently an ideal quasi-free-standing monolayer has been realized [30]. Further, silicon intercalation has been introduced to reduce the interaction between the phosphorus and the metallic substrate [34]. These experimental advances pave a solid foundation for further exploration of the applications of blue phosphorene. On the other hand, an accurate first-principles approach to the electronic and optical properties of 2D materials is nontrivial. Compared with bulk materials, the dielectric screening in 2D materials shows a nonmonotonic  $\mathbf{q}$  (or distance) dependence [35–51]. The quasiparticle band-correction and exciton effects on optical

\*caitianyi@suda.edu.cn

†jusheng@suda.edu.cn

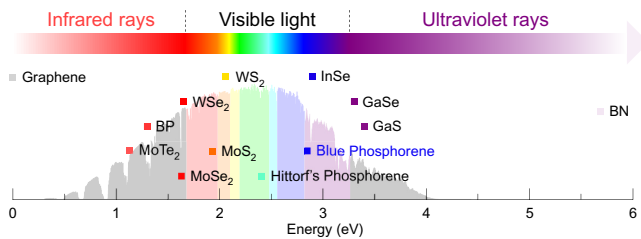


FIG. 1. Some 2D materials covering a broad spectral range, from zero-band-gap graphene to narrow-band-gap BP, an intermediate-band-gap TMD monolayer, and wide-band-gap semiconductors of Hittorf's phosphorene, blue phosphorene, a III–VI monochalcogenides monolayer, and a BN monolayer. The solar spectrum is also shown [11].

properties are very crucial. The indirect band gap of blue phosphorene makes an accurate approach to the determination of the excitonic properties extremely computationally expensive [16–20]. In this paper, based on systematic first-principles studies with the advanced *GW*-BSE method (where BSE refers to the Bethe-Salpeter equation), we study the quasiparticle electronic structure, exciton, and optical properties of blue phosphorene and their strain dependence. It is revealed that the indirect band gap in pristine blue phosphorene can be effectively tuned toward an almost direct one via sufficient tensile strain. Furthermore, the optical absorption spectrum exhibits an obvious red shift when the lattice constant increases. Similar to other 2D materials, the optical spectrum is dominated by strong bound excitons. The exciton binding energy could reach as high as 0.9 eV. The relationship between the band gap and the exciton binding energy as exhibited in these strained systems is, however, illusory. It is revealed that

the larger the quasiparticle band gap is, the smaller is the exciton binding energy. This unusual dependence is found to be accompanied by an enhanced effective mass of the excitons and decreased dielectric screening when the lattice constants are increased. Interestingly, such an unusual strain dependence of the electronic and excitonic properties in blue phosphorene could be utilized to realize a funnel effect by imposing an inhomogeneous strain in a 2D membrane, which could be useful for green and blue LED techniques in 2D materials. Our findings not only provide a deep understanding of the fundamental relationship between the band gap and the dielectric screening, exciton, and optical properties in 2D materials, but also show the potential application of this wide-band-gap semiconductor blue phosphorene in 2D optoelectronics.

## II. COMPUTATIONAL METHOD

Our first-principles calculations of blue phosphorene are performed using density-functional theory (DFT) as implemented in the QUANTUM ESPRESSO software [52]. The quasiparticle band structure and optical properties are calculated using the BerkeleyGW software package [53–55]. A slab model is used, with a vacuum layer of 16 Å along the out-of-plane direction. In the meantime, a truncated Coulomb interaction between the blue phosphorene and its periodic image is adopted. The quasiparticle self-energies are obtained by solving the following Dyson equation:

$$\left[ -\frac{1}{2} \nabla^2 + V_{\text{ion}} + V_H + \Sigma(E_{n\mathbf{k}}^{\text{QP}}) \right] \psi_{n\mathbf{k}}^{\text{QP}} = E_{n\mathbf{k}}^{\text{QP}} \psi_{n\mathbf{k}}^{\text{QP}}, \quad (1)$$

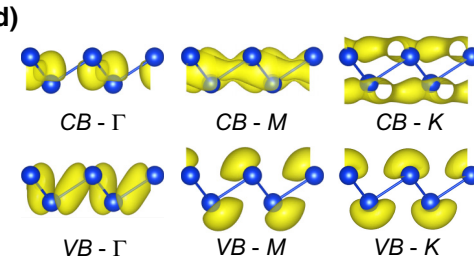
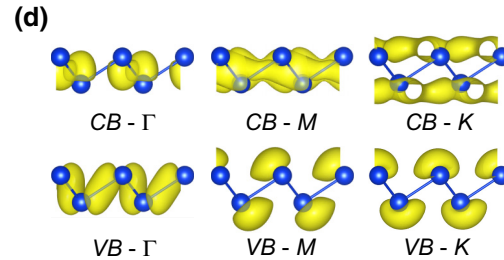
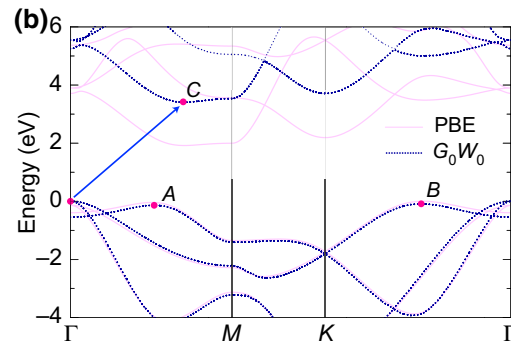
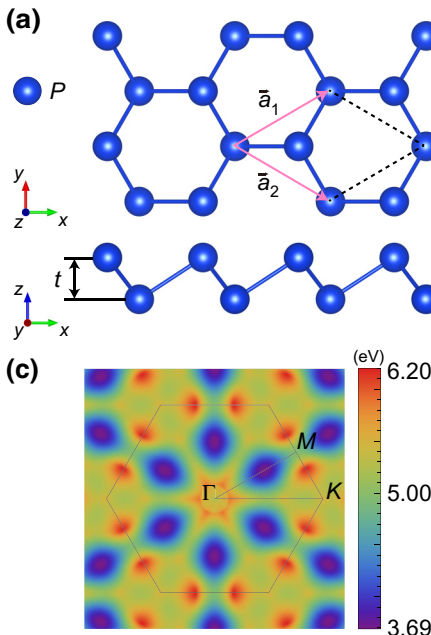


FIG. 2. (a) The crystal structure of blue phosphorene. (b) The quasiparticle electronic band structure of blue phosphorene from the  $G_0W_0$  approximation (dotted blue curve) and PBE (solid pink curve), respectively. The indirect band gap is indicated by the arrow. (c) The lowest direct band-to-band transition energies ( $G_0W_0$ ) in the Brillouin zone. (d) The orbitals of the highest valence band (VB) and the lowest conduction band (CB) at high-symmetry  $k$  points.

where  $\Sigma$  is the self-energy operator within the  $GW$  approximation and  $E_{n\mathbf{k}}^{\text{QP}}$  and  $\psi_{n\mathbf{k}}^{\text{QP}}$  are the quasiparticle energies and wave functions, respectively. We use the  $G_0W_0$  level with a generalized plasmon pole model.

The static polarizability is calculated by random-phase approximation from

$$\begin{aligned} \chi_{GG'}(\mathbf{q}; 0) = & \sum_{n, n', \mathbf{k}} \langle n, \mathbf{k} | e^{-i(\mathbf{q} + \mathbf{G}) \cdot \mathbf{r}} | n', \mathbf{k} + \mathbf{q} \rangle \\ & \times \langle n', \mathbf{k} + \mathbf{q} | e^{i(\mathbf{q} + \mathbf{G}) \cdot \mathbf{r}'} | n, \mathbf{k} \rangle \frac{1}{E_{n\mathbf{k}+\mathbf{q}} - E_{n'\mathbf{k}}}, \end{aligned} \quad (2)$$

where  $n$  and  $n'$  are occupied and unoccupied band indices,  $\mathbf{k}$  is the wave vector,  $\mathbf{q}$  is a vector in the first Brillouin zone,  $\mathbf{G}$  is a reciprocal-lattice vector, and  $\langle n, \mathbf{k}$ , and  $E_{n\mathbf{k}}$  are the mean-field electronic eigenvectors and eigenvalues.

Then, the dielectric matrix is constructed as follows:

$$\epsilon_{GG'} = \delta_{GG'} - v(\mathbf{q} + \mathbf{G}) \chi_{GG'}(\mathbf{q}; 0), \quad (3)$$

where  $v(\mathbf{q} + \mathbf{G}) = 4\pi/|\mathbf{q} + \mathbf{G}|^2$  is the bare Coulomb interaction.

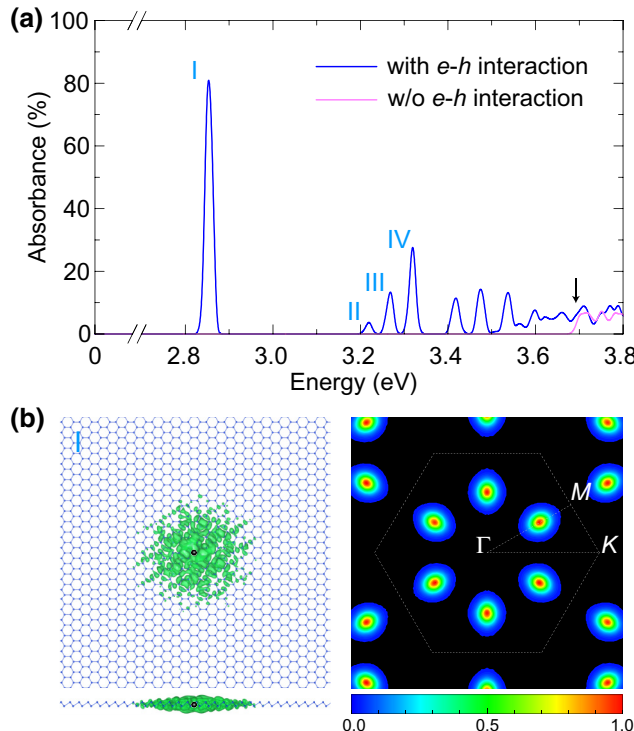


FIG. 3. (a) The optical absorbance of blue phosphorene with (blue line) and without (pink line) electron-hole interactions using a constant broadening of 5 meV. The arrow indicates the quasiparticle band gap. (b) Real-space (left panel) and reciprocal-space (right panel) plots of the modulus squared of the 1s exciton wave function. The hole (black circle) is fixed at the center of the bond between two neighboring phosphorus atoms.

The electron-hole excitations are then calculated by solving the BSE for each exciton state  $S$ :

$$\left( E_{c\mathbf{k}}^{\text{QP}} - E_{v\mathbf{k}}^{\text{QP}} \right) A_{vc\mathbf{k}}^S + \sum_{v'c'\mathbf{k}'} \langle vc\mathbf{k} | K^{eh} | v'c'\mathbf{k}' \rangle = \Omega^S A_{vc\mathbf{k}}^S, \quad (4)$$

where  $A_{vc\mathbf{k}}^S$  is the exciton wave function,  $\Omega^S$  is the excitation energy, and  $K^{eh}$  is the electron-hole interaction kernel. Finally, we obtain the imaginary part of the frequency-dependent complex dielectric function  $\epsilon_2(\omega)$  as

$$\epsilon_2(\omega) = \frac{16\pi^2 e^2}{\omega^2} \sum_S |\mathbf{e} \cdot \langle 0 | \mathbf{v} | S \rangle|^2 \delta(\omega - \Omega^S), \quad (5)$$

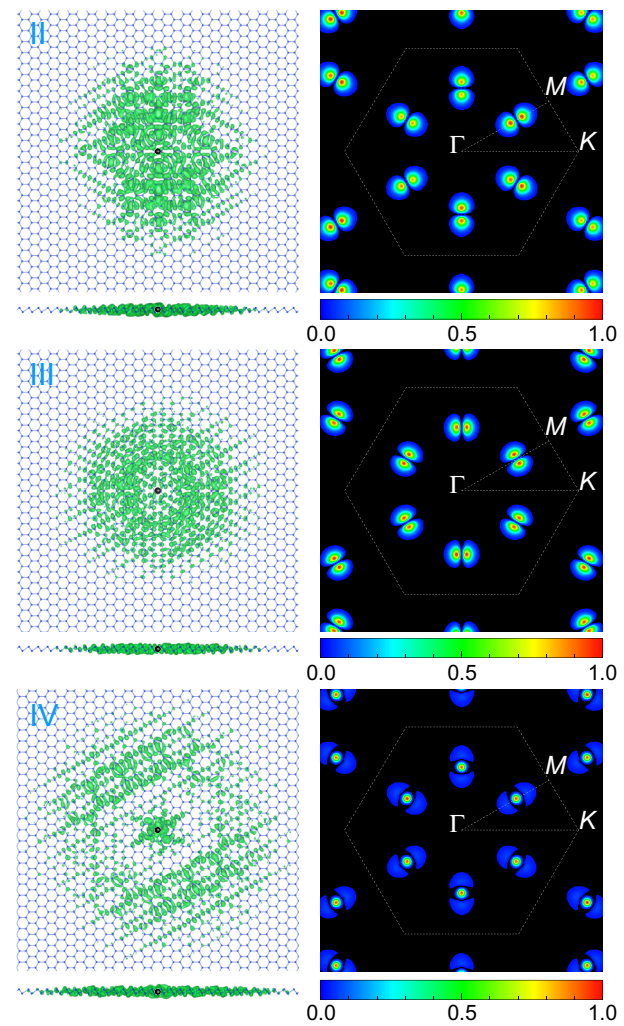


FIG. 4. Real-space plots of the modulus squared of the exciton wave function (left panel) and reciprocal-space plots (right panel) for the second, third, and fourth absorption peaks. Here, the hole (black circle) is fixed at the center of the bond between two neighboring phosphorus atoms.

where  $\mathbf{v}$  is the velocity operator and  $\mathbf{e}$  is the polarization of the incoming light. Here, we use the absorbance  $A$  of 2D materials to measure its optical properties: it is expressed as

$$A(\omega) = 1 - e^{-\alpha(\omega)d} = 1 - e^{-\omega\epsilon_2 d/\hbar c}, \quad (6)$$

where  $\alpha$  is the absorption coefficient,  $d$  is the thickness of the simulation cell along the direction perpendicular to the layer,  $\epsilon_2$  is the imaginary part of the dielectric function, and  $\omega$  is the photon energy. Here, considering that most of the area in the simulation cell is vacuum, we approximate the absorption coefficient by using the refractive index  $n = 1$  of vacuum. We use the Perdew-Burke-Ernzerhof (PBE) [56] generalized gradient approximation and norm-conserving pseudopotentials with a plane-wave cutoff of 60 Ry [57]. For the convergence of the quasiparticle energies [58], we test the dependence on the  $k$  grid size and the number of bands, as well as the dielectric cutoff (see Appendix A). We use a coarse  $k$  grid of  $30 \times 30 \times 1$  and 495 empty bands, with the highest unoccupied state at 8.4 Ry (five occupied bands, with the lowest occupied state at  $-1.3$  Ry) and a dielectric cutoff of 10 Ry. For the BSE part, a fine  $k$  grid of  $120 \times 120 \times 1$  is used (see Appendix A). It is noted that fine sampling is necessary to capture the rapid variation in screening at small wave vectors and the fine features in the exciton wave functions, which are tightly localized in  $k$  space. We use Gaussian smearing with a broadening constant of 5 meV in the optical absorption spectrum. The number of bands for the optical transitions is three for both the valence and the conduction bands, which is sufficient to cover the span of the visible light.

### III. RESULTS AND DISCUSSION

#### A. Pristine blue phosphorene

While sharing the atomic connectivity with the honeycomb lattice of graphene, the crystal structure of blue phosphorene is nonplanar. As shown in Fig. 2(a), there are two atomic sites in the primitive cell of blue phosphorene. The lattice constant (theoretically optimized) is 3.28 Å with a P—P bond of 2.26 Å. The effective thickness  $t$  is 1.24 Å. Electron self-energy effects computed at the  $G_0W_0$  level modify the band structure strongly. The quasiparticle band structure of blue phosphorene, as shown in Fig. 2(b), reveals that it is an indirect-band-gap semiconductor with a band gap of 3.41 eV (indicated by the arrow). The band gaps at the high-symmetry  $k$  points  $\Gamma$ ,  $M$ , and  $K$  are 5.25, 4.95, and 5.52 eV, respectively. The top of the valence states is located at point  $\Gamma$  and the bottom of the conduction states is located along the path from point  $\Gamma$  to point  $M$ , which we label as point  $C$ . We also label two local maxima at the top of valence bands, i.e., points  $A$  and  $B$ . In contrast, the band gap is underestimated at the PBE level with a magnitude of 1.92 eV and the top of the valence

bands is found to be located at point  $B$ . It is noted that our calculation of the quasiparticle band gap is consistent with previous  $G_0W_0$  results of 3.53 eV [16] and 3.36 eV [19]. The energies for the direct transitions from the highest valence band to the lowest conduction band are shown in Fig. 2(c). Six deep valleys of 3.69 eV are found in the first Brillouin zone. The local partial charges are plotted in Fig. 2(d) and are consistent with the maximum localized Wannier-orbitals analysis (see Appendix B) [59]. The  $3p$  orbitals in the  $x$ - $y$  plane and along the  $z$  direction interact with each other from two atomic sites. The density of states of the top of the valence bands is very large, providing a good possibility of efficient hole-injection in this 2D system (see Appendix B).

The optical absorption spectrum is shown in Fig. 3(a). When the electron-hole interactions are considered, the optical absorption spectrum is found to be modified dramatically due to the exciton effect. For blue phosphorene, the first two excitonic states ( $1s$ ) give rise to the first optical absorption peak (peak I at 2.85 eV). The exciton binding energy is 0.84 eV, which is similar to that in MoS<sub>2</sub> [38,39,41,47] and BP [40,42,43,50]. The absorption peaks II at 3.22 eV, III at 3.27 eV, and IV at 3.32 eV show much smaller optical absorption magnitude. The exciton states for these optical responses also exhibit a smaller binding energy of around 0.5 eV. The character of the excitons giving rise to these low-energy peaks in the absorption spectrum is studied by the plot of the exciton wave function.

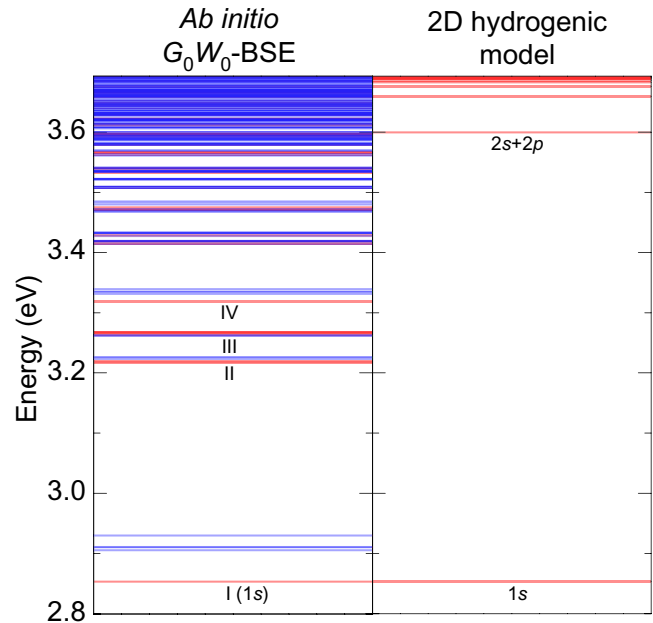


FIG. 5. The excitonic states obtained from  $G_0W_0$ -BSE (left panel) in comparison with the 2D hydrogenic model (right panel), with a uniform dielectric screening obtained from the fitting of the  $1s$  excitonic state. The red lines are for the bright exciton states and the blue lines are for the dark exciton states.

The exciton states for peak I are from the combinations of the free electron-hole transitions centered at six valleys, as indicated above. The wave functions of these two excitons look identical in real space. In Fig. 3(b), we show the modulus squared of the real-space exciton wave function. The hole is fixed at the center of the P—P bond. The character of the exciton corresponding to peak I reflects the P 3p orbitals of the states in the lowest blue phosphorene conduction band. The envelope of the exciton wave function is almost azimuthally symmetric. The root-mean-square radius of the exciton in real space is around 1 nm. On the other hand, the  $k$ -space plot shows that the transitions are highly localized around the six valleys with the lowest transition energy. The excitons corresponding to peaks II, III, and IV are shown in Fig. 4. Compared with the 1s state, these excitons possess a much increased real-space extension of the wave function. The effective electron-hole interaction is therefore reduced strongly, consistent with the smaller binding energy revealed above. The reciprocal space plot of the exciton wave function is also located around the valleys. However, unlike the 1s state, these nodelike shapes show the characteristics of a higher order of excitations.

The exact exciton energies are shown in Fig. 5, where peak I is made up of two energetically degenerate excitons, which are bright. Furthermore, at slightly higher energies above, four dark excitons are found, consistent with

six valleys of the lowest optical transitions. Clearly, our  $G_0W_0$ -BSE exciton spectrum is completely different from that of a 2D hydrogen model, again verifying the nonuniform (state-dependent) dielectric screening and the nature of the nonhydrogenic Rydberg series of excitons in 2D materials, e.g., MoS<sub>2</sub> [47], and the  $q$  dependence of the dielectric screening in blue phosphorene. The model due to Ref. [35–37,40], improved by considering the  $q$ -dependent dielectric screening, could give reasonable exciton states and show good agreement with experiments and  $GW$ -BSE results. Here, the exciton states are schematically built by fitting the 1s-state energy obtained in our first-principles calculations with  $E_n \propto (n - 1/2)^{-2}$ . In the meantime, the dark excitons have an oscillation strength less than  $10^{-5}$ . For example, the first dark exciton at 2.91 eV has an oscillation strength of  $10^{-7}$ , which corresponds to an optical absorbance of less than 0.001%.

## B. Biaxial strain effect

Based on the above discussions, it is obvious that blue phosphorene is an indirect wide-band-gap semiconductor and that its optical properties are dominated by strong bound excitons. For 2D materials, the strain is found to be an effective way to tune the quasiparticle electronic structure, excitons, and optical response [49]. It is interesting to study the strain effect in blue phosphorene further.

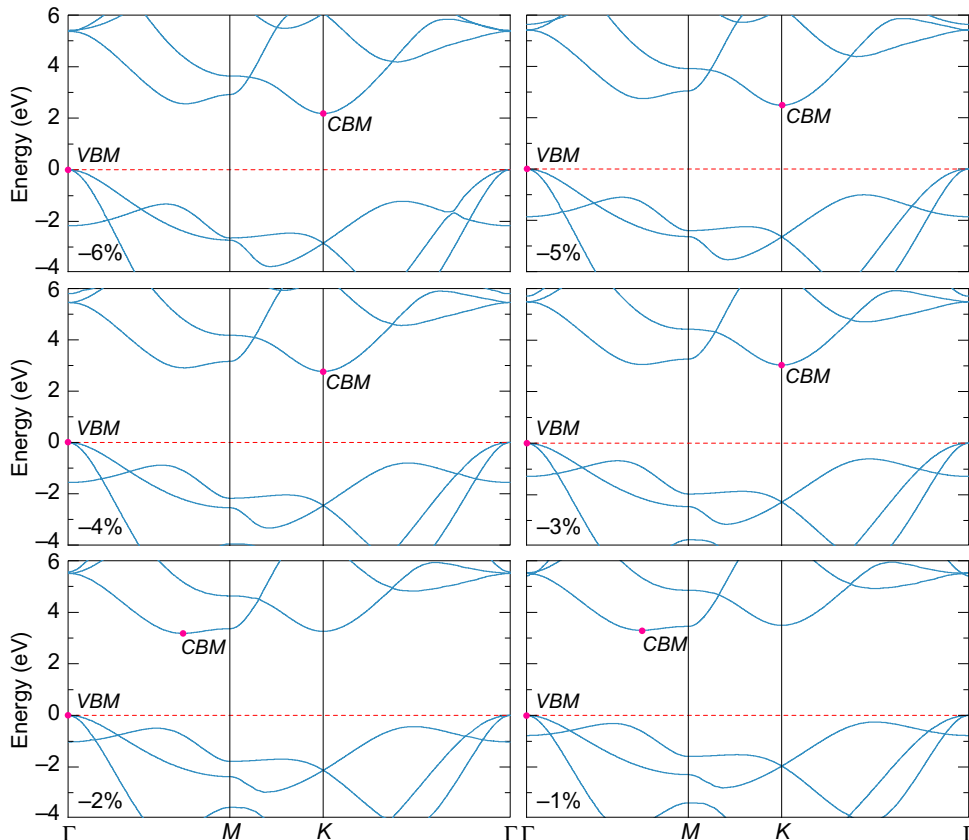


FIG. 6. The quasiparticle band structure ( $G_0W_0$ ) of compressively-strained blue phosphorene.

At the PBE level, it has been revealed that the strain could change the indirect band gap in blue phosphorene strongly [15] (also see Appendix C). In Figs. 6 and 7, we first demonstrate the strain dependence of the quasiparticle band structure of blue phosphorene under biaxial strain for compressive and tensile strain, respectively. When the lattice constant is increased, the top of the valence band changes from point  $\Gamma$  point to point  $B$ . The bottom of the conduction band is fixed at the original point  $C$ . When the tensile strain is applied progressively, the energy difference between points  $A$  and  $B$  gets smaller and smaller and the system is an almost direct-band-gap semiconductor when the tensile strain reaches 5% [see Fig. 8(a) for the energy difference between  $A$  and  $B$ ]. On the other hand, for compressive-strained systems, the top of the valence band is still located at point  $\Gamma$ . The plots of the direct lowest transition energies indicate that the spatial extension of the six valleys gets larger in the BZ when the lattice constant is increased (see Fig. 9). In the meantime, the absolute value of the lowest transition decreases.

To connect the band structure with the optical transitions and excitonic states clearly, we show the details of the electron-hole transitions composing the 1s exciton (corresponding to peak I in the optical absorption spectrum) in Fig. 10. The center is labeled as point  $\Lambda$  and the half-height width is shown with a series of arrows of decreasing strength. The relative energy differences between point  $A$

(the top of the valence bands), point  $C$  (the bottom of the conduction band), and the  $\Lambda$  values and their evolution with strain can be easily judged. In Figs. 8(b) and 8(c), we can find that these relative energy differences are very small (around 10 meV for the tensile-strained systems), indicating feasible carrier injection for direct electron-hole recombination and, consequently, efficient light emission in these systems.

The evolution of the exact band gaps with the strain is shown in Fig. 11. Obviously, as shown in Fig. 11(a), the indirect band gap decreases with a decreasing lattice constant for compressive strain, while it increases with an increasing lattice constant for tensile strain. The indirect band gap shows a maximum near the pristine system, with a little tensile strain. However, at the PBE level (Appendix C), the maximum is close to the compressive side. On the other hand, as shown in Fig. 11(b), transitions (mainly at point  $\Lambda$ ) corresponding to the first absorption peak decrease monotonically with an increase in the lattice constant under both compressive and tensile conditions. This is similar to the PBE results. These findings demonstrate the unique aspects of the electronic structure of indirect-band-gap semiconductors.

The evolution of the optical absorbance with the strain is shown in Fig. 12. There is an obvious red shift of the absorption edge when the lattice constant is increased. The span is significant, which is useful for optoelectronics

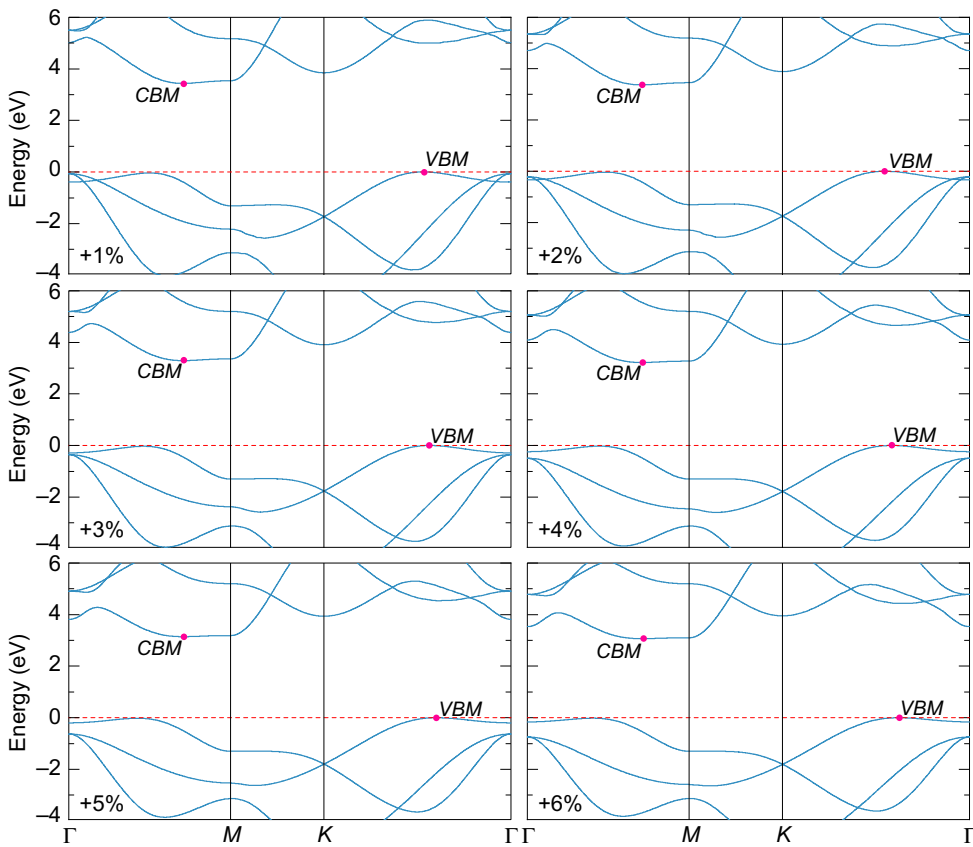


FIG. 7. The quasiparticle band structure ( $G_0W_0$ ) of tensile-strained blue phosphorene.

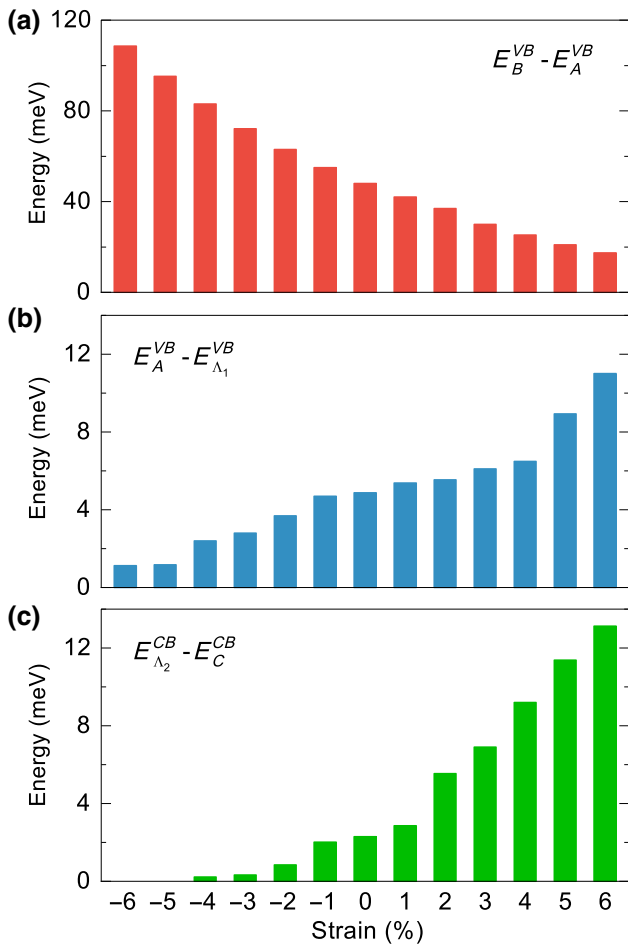


FIG. 8. The strain dependence of the quasiparticle energy differences between some special  $k$  points. (a)  $A$  and  $B$  for the location of the top of the valence bands. (b)  $\Lambda_1$  (indicated in Fig. 10 for optical transitions around the 1s exciton) and  $A$  (the top of the valence bands). (c)  $\Lambda_2$  (indicated in Fig. 10 for optical transitions around the 1s exciton), and  $C$  (the bottom of the conduction bands).

applications. In particular, when the lattice constant is increased up to 6%, the absorption edge changes from its original value of 2.8 eV to 2.4 eV, covering violet, blue, and green light. In the meantime, the magnitude of the first absorption peak is almost invariable, indicating the unchanging strong oscillation strength of these optical excitations.

The evolution of the exciton properties is further shown in Fig. 13, where both the exciton binding energy and the effective mass (1s state) increase when the lattice constant is increased. In general, it is believed that in 2D materials, the larger the band gap is, the stronger is the binding energy [44,46,48]. A similar relationship is believed to exist between the band gap and effective mass of excitons. However, for blue phosphorene, the larger the band gap is, the weaker the binding energy is revealed to be. In the meantime, the larger the band gap is, the smaller is

the effective mass. This unusual dependence is intriguing. To understand this point, we resort to dielectric screening. In Fig. 14(a), we show the  $\mathbf{q}$  dependence of the dielectric function. Similar to other 2D materials, the screening increases first from unity ( $\epsilon_0$ ) for the long-wavelength limit and then decreases for short distances. Clearly, when the lattice constant is increased, the dielectric screening is reduced systematically. In 2D systems, the dielectric function is well known for its intrinsic  $\mathbf{q}$  dependence in the form  $\epsilon(\mathbf{q}) = 1 + 2\pi\alpha\mathbf{q}$ , where  $\alpha$  is the polarizability. The 2D polarizability  $\alpha$  is obtained by fitting the above equation to the long-wavelength limit ( $\mathbf{q} \rightarrow 0$ ) of our calculated  $\mathbf{q}$  dependence of  $\epsilon$ . A decrease of the polarizability is evident in Fig. 14(b). This solid evidence is consistent with the decreased exciton binding energy and strongly suggests that in 2D materials, the band gap might be not the unique indicator of the magnitude of the exciton binding energy. In particular, for the indirect-band-gap system, the exact dielectric screening arising from all the transitions in the whole BZ is evaluated without bias [see Eq. (2)].

To access the excitonic properties of blue phosphorene further, we calculate the lifetime of the 1s bright exciton. Using Fermi's golden rule, the radiative lifetime  $\tau_S(0)$  at 0 K of an exciton in state  $S$  is derived according to [60,61]

$$\tau_S(0) = \frac{\hbar^2 c}{4\pi e^2 E_S(0)} \frac{A_{\text{u.c.}}}{\mu_S^2}, \quad (7)$$

where  $c$  is the speed of light,  $A_{\text{u.c.}}$  is the area of the unit cell,  $E_S(0)$  is the energy of the exciton in state  $S$ , and  $\mu_S^2 = [\hbar^2/m^2 E_S(0)^2] (|\langle G|p_{||}|\Psi_S\rangle|^2/N_k)$  is the square modulus of the BSE exciton transition dipole divided by the number of unit cells in this 2D system. We obtain the exciton radiative lifetime  $\langle\tau_S\rangle$  at temperature  $T$ :

$$\langle\tau_S\rangle = \tau_S(0) \frac{3}{4} \left( \frac{E_S(0)^2}{2M_S c^2} \right)^{-1} k_B T, \quad (8)$$

where  $k_B$  is the Boltzmann constant and  $M_S = m_e^* + m_h^*$  is the exciton mass.

The exciton lifetime of the lowest-energy exciton at room temperature (300 K) is 0.24 ns. Compared with conventional wide-band-gap LED materials, e.g., a (Ga,In)N/GaN quantum well with a radiative lifetime around  $10^2$  ns [62], the relatively short lifetime in blue phosphorene shows its advantage in LED applications. As shown in Fig. 15, for the strain dependence of the exciton lifetime, the value increases a little when the lattice constant is increased, e.g., 0.63 ns for a 6% strained system. The relatively short lifetime in 2D materials, e.g., 18 ns in Hittorf's phosphorene [14], 0.002 ns in BP [63], around 1 ns in TMDs [64–70], and 0.6 ns in 2D GaN [51], is beneficial to the radiative process of excitons in LED techniques.

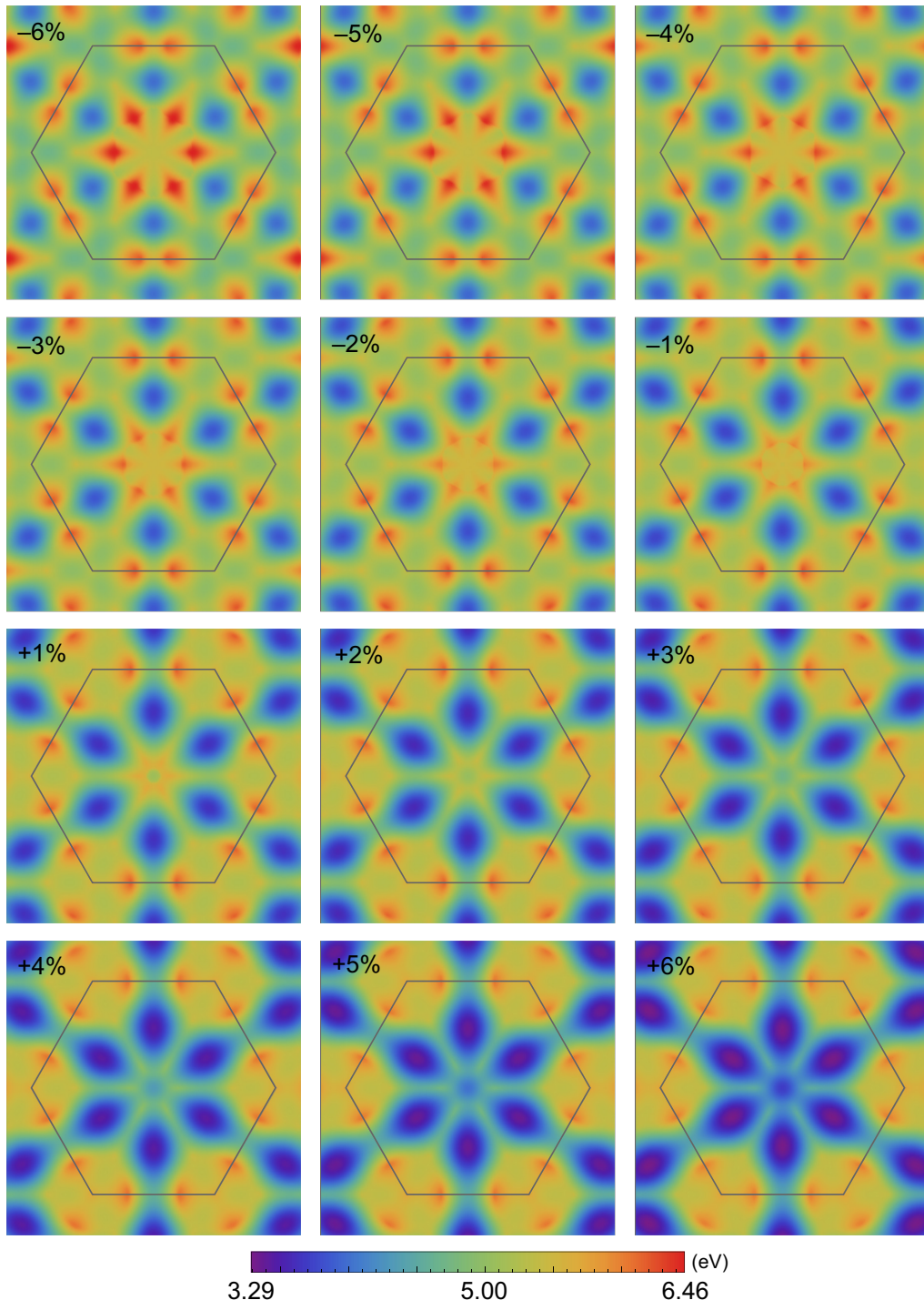


FIG. 9. The direct band gaps in the BZ ( $G_0W_0$ ) for the strained blue phosphorene.

### C. Funnel effect for a 2D optoelectronic device based on inhomogeneously strained blue phosphorene

With the above analysis, it is interesting to explore the potential applications of blue phosphorene in 2D optoelectronics. As for those already implemented in TMDs [71–73], an illustration of a 2D optoelectronic device based on blue phosphorene with split gate electrodes is shown in Fig. 16(a). Two gate electrodes couple to different regions

of the layer. First, biasing one gate with a negative voltage ( $V_{G1}$ ) and the other with a positive voltage ( $V_{G2}$ ) will attract holes and electrons, respectively, and thus a *p-n* junction is formed. By using a source-drain voltage ( $V_{SD}$ ), the electrons and holes transported in antiparallel directions can recombine in the junction and emit photons, making the device operate as an LED. Similarly, when operating as a solar cell or photodiode, with the incident

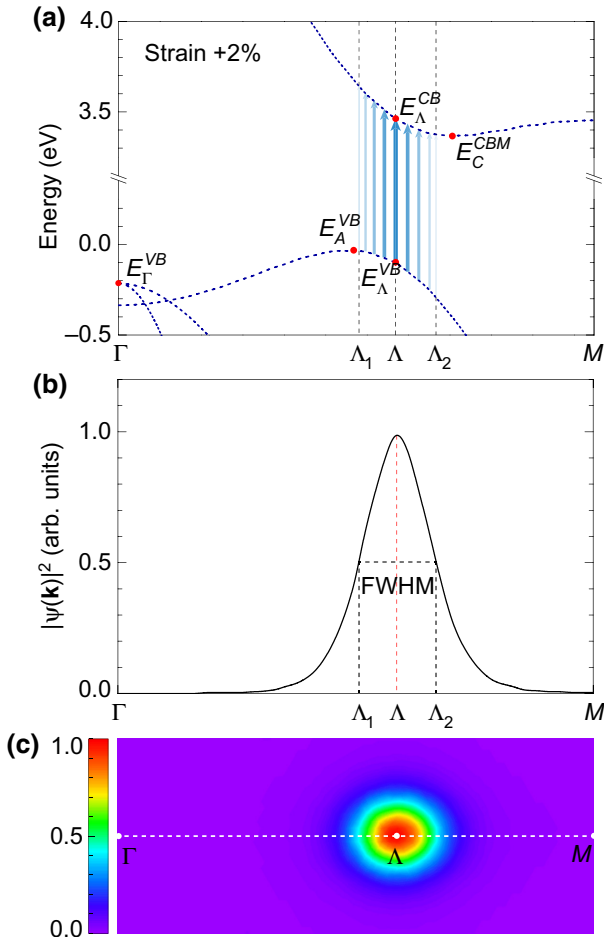


FIG. 10. (a) The quasiparticle band structure and optical transitions of the 1s excitonic state with their distribution in the BZ. Here, we use +2% strained blue phosphorene as an example, where the top of the valence band at point  $\Gamma$  is lower than that at point  $A$ . (b) The reciprocal-space plot of the modulus squared of the 1s exciton wave function along the path from point  $\Gamma$  to point  $M$ . (c) The 2D plot corresponding to (b).

light absorbed in this *p-n* junction, a photocurrent and photovoltage will be generated. Such a 2D monolayer *p-n* junction is very effective in photovoltaic solar cells, photodiodes, and LEDs, overcoming many limitations (e.g., rigidity, heavy weight, and high cost) of conventional bulk semiconductors. Due to its strong optical absorbance and strain-tunable optical absorption edges, blue phosphorene could be suitable for application to 2D solar cells.

Interestingly, the above-revealed strain dependence of the band structure, excitonic, and optical properties in blue phosphorene could be an additional tunability factor and could be used to enhance the efficiency of this 2D device further. As shown in Fig. 16(a), when an inhomogeneous strain is imposed, the center with the maximum tensile strain applied shows the lowest band gap. For the relative alignment of the band edges, as shown in Fig. 16(b), the center behaves as the top of valence band as well as

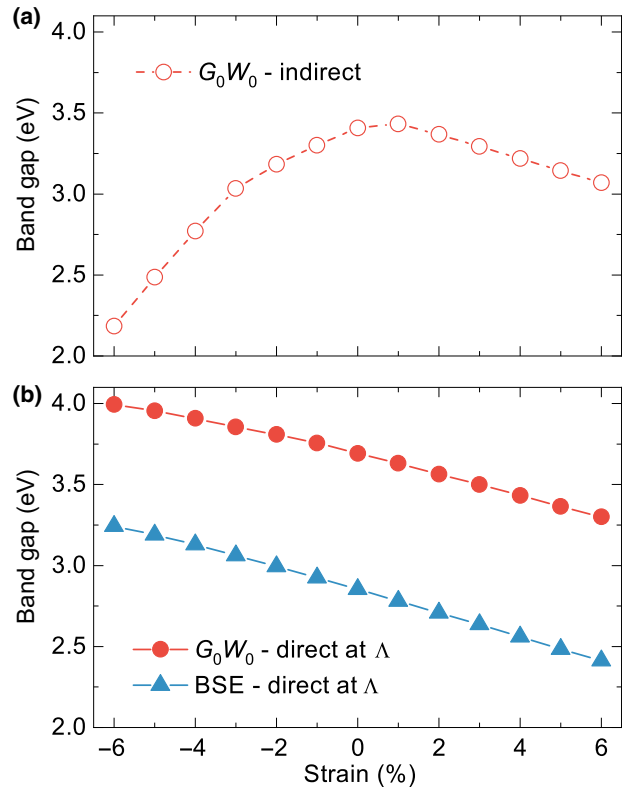


FIG. 11. The evolution of the band gaps in blue phosphorene with biaxial strain. (a) The quasiparticle ( $G_0W_0$ ) indirect band gap. (b) The direct quasiparticle ( $G_0W_0$ ) and optical (BSE) band gap at point  $\Lambda$ .

the bottom of the conduction band of the whole 2D membrane. Therefore, in this inhomogeneously strained blue phosphorene, either gate-controlled carriers or photoexcited electron-hole pairs at other less strained locations will spontaneously drift toward the center and a funnel effect is

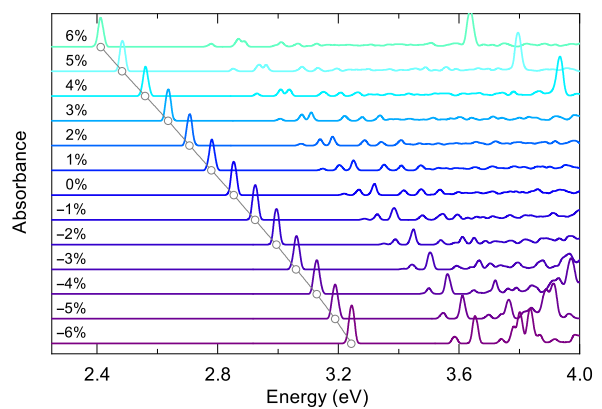


FIG. 12. The evolution of the optical absorbance in blue phosphorene with biaxial strain. The color corresponds to the energy of the first absorption peak.

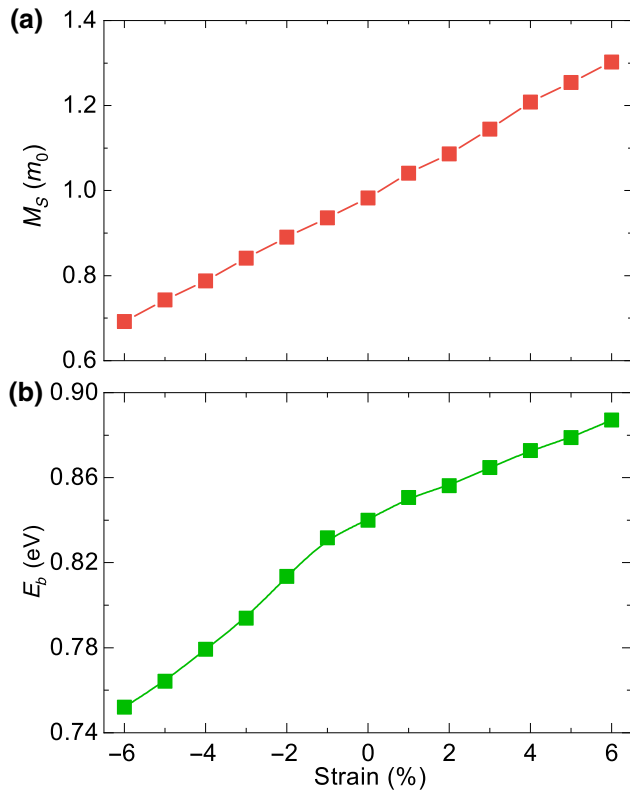


FIG. 13. The evolution of (a) the exciton effective mass and (b) the binding energy in blue phosphorene with biaxial strain.

realized. Notably, the center possesses stronger electron-hole binding energy than other less strained locations, making the funnel efficient when acting as a light-emitting diode. Such a kind of design could compensate for the indirect-band-gap nature of blue phosphorene, where the indirect transition could reduce the electron-hole recombination and consequently the LED efficiency. This scenario is very similar to the design strategy in bulk semiconductor GaP-N [74–81]. As is well known, GaP is an indirect-band-gap semiconductor. At very low concentrations ( $10^{16} \text{ cm}^{-3}$ ), an isolated N introduces a highly localized state in GaP, where the energy level is located slightly below the conduction-band minimum. Such a spatial localization leads to a quasidirect transition in GaP-N. In other words, the nitrogen impurity binds the exciton, localizing the wave function in real space and causing it to spread out in  $k$  space. The  $k$ -space delocalization allows the  $k$ -space overlap between the electron and hole necessary for direct recombination and efficient LED devices. The funnel effect realized in an inhomogeneously strained blue phosphorene 2D membrane behaves similarly toward the maximum overlap between the wave functions of injected electron and holes. This method may be suitable for other indirect-band-gap 2D materials, where the presence of indirect channels leads to low photoluminescence (see Appendix D) [22,23]. In TMDs [82] and BP [83],

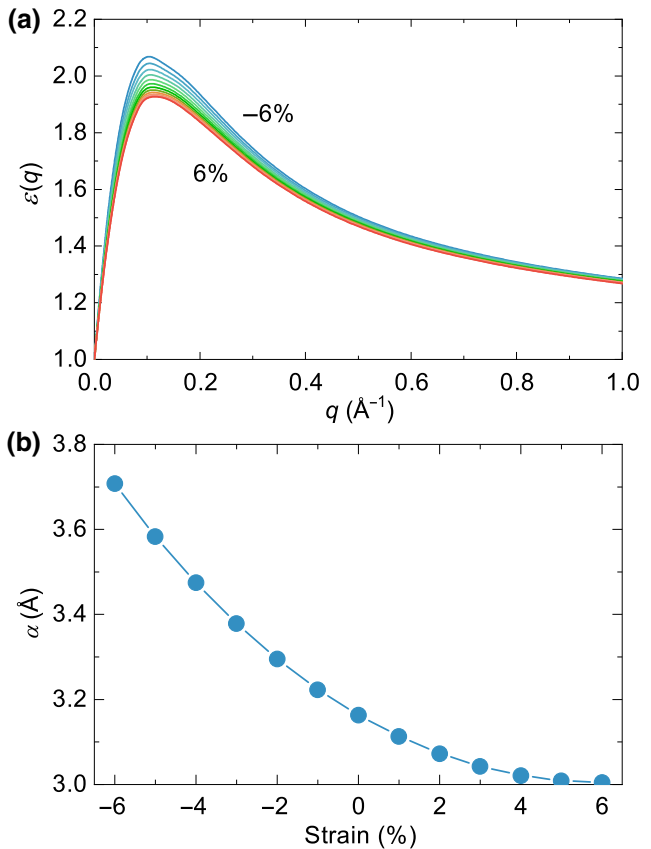


FIG. 14. The evolution of dielectric screening in blue phosphorene with biaxial strain. (a) The  $q$  dependence of dielectric constant. (b) The 2D polarizability.

the funnel effect and the inverse funnel effect have been revealed, respectively. In TMDs, e.g., MoS<sub>2</sub>, the larger the band gap is, the larger is the binding energy [49,82]. In BP, the same relationship has been revealed [83]. This means that in both TMDs and BP, the electron-hole binding strength is weakest at the band edges, which is beneficial to

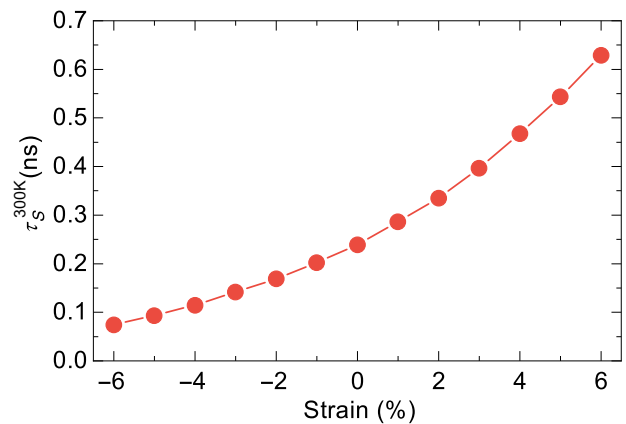


FIG. 15. The evolution of the exciton lifetime at room temperature in blue phosphorene with biaxial strain.

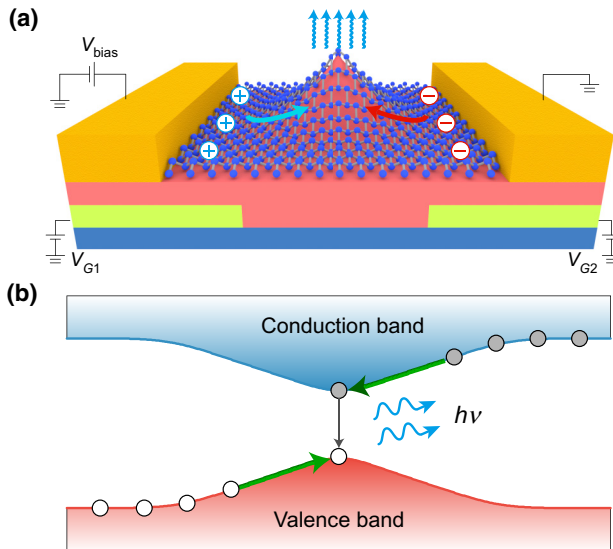


FIG. 16. (a) An illustration of a gate-tunable 2D optoelectronic device for photon detection, energy conversion, and light emission. The blue phosphorene is subjected to an inhomogeneous strain tuned by proper design of the geometry of the substrate. (b) The corresponding energy profile of the electron and hole for the funnel effect. Here, the center with the maximum strain imposed behaves as the band edges and has the strongest exciton binding energy.

the electron-hole separation and the photovoltaic harvest. Therefore, with the proper design of the strain profile, blue phosphorene could act as a 2D optoelectronic device for green and blue LEDs.

To simulate the strain field needed to generate the funnel effect in experiments, we adopt the Föppl-Hencky equation to compute the morphology and the strain distribution of monolayer blue phosphorene under the proposed experimental setup [84–86]. The Föppl-Hencky equation is appropriate to describe isotropic circular membrane systems such as blue phosphorene with a  $D_{3d}$  point group. In our simulation, we investigate a system of an edge-clamped circular membrane with a spherical indentation in frictionless contact, using an exact method to calculate the analytical solution of the Föppl-Hencky equation [87]. This method gives the solution in two regions: the free region of the membrane that is noncontacting and

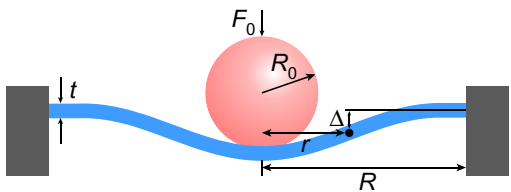


FIG. 17. A simulation of the experimental setting of a 2D membrane of blue phosphorene under indentation.

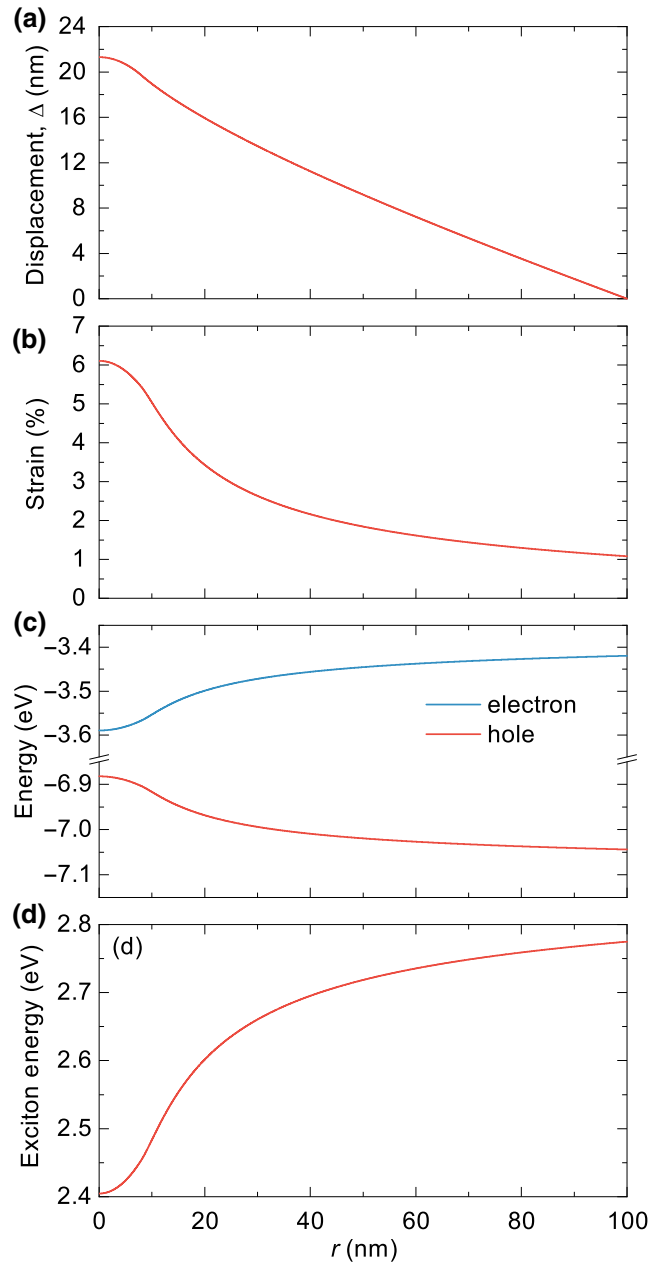


FIG. 18. The profile of (a) the perpendicular displacement, (b) the strain field, (c) the band edge, and (d) the exciton excitation energy in a membrane of 2D blue phosphorene.

the region of the membrane that is in frictionless contact with the indenter. We assume the following experimental settings, as shown in Fig. 17, with a radius  $R$  of the membrane of 100 Å, a radius of the indenter ( $R_0$ ) of 20 Å, and an indentation force ( $F_0$ ) of 30 nN, which are in the appropriate range as described in the similar experimental settings for indentation for a circular membrane [82,88]. The Young's modulus of 203 GPa and the Poisson ratio of 0.11 are obtained within DFT calculations of blue phosphorene.

The relationship between the vertical displacement  $\Delta$  and the radius  $r$  is shown in Fig. 18(a). The displacement starts to increase from the boundary and reaches a maximal displacement of 21.3 Å. The radial strain distribution is shown in Fig. 18(b), exhibiting nonuniform characteristics and a maximal value of 6.11% in the center. The strain and its gradient increase quickly from the boundary, causing the strain to mainly be confined in the center area of the membrane, in frictionless contact with the indenter.

After calculating the strain field in the monolayer blue phosphorene, we can derive the energy profile of the quasiparticle band edges and the exciton by interpolating the results for blue phosphorene under biaxial strain in the main text. The interpolated band edges of electrons and holes are shown in Fig. 18(c). The band edges of the electrons and holes are shifted in the reverse direction and the band gap is decreasing toward the center of the membrane. The energy profile of the lowest exciton is shown in Fig. 18(d), which has a trend similar to that of the strain field. The consistency is the result of the almost linear relationship between the optical band gap and the strain, as shown in Fig. 18(b). Clearly, the funnel proposed above can be safely realized in the current laboratory setup.

#### IV. SUMMARY AND CONCLUSIONS

To summarize, by studying the strain dependence of the quasiparticle electronic structure, exciton, and optical properties of blue phosphorene, we reveal a funnel effect in this 2D wide-band-gap semiconductor. The enhanced many-body effects arising from the 2D quantum confinement and the unique 2D dielectric screening are captured well in our first-principles  $GW$ -BSE calculations. Considering a  $p$ - $n$  diode device for 2D materials, the designed funnel structure with inhomogeneous strain could be used to accelerate the drift of electrons or holes toward the center. In the meantime, the available intrinsic strong oscillation strength, the large binding energy, and the relatively short radiative lifetime in blue phosphorene provide obvious advantages over conventional wide-band-gap semiconductors in green and blue LEDs. The key advantage of this strain-engineered device is its tunability. The region in which the electron-hole radiative recombination occurs and the frequency of the emission can be tuned flexibly by adjusting the applied strain.

#### ACKNOWLEDGMENTS

S.J. thanks Professor Steven G. Louie and all his group members for their valuable assistance on the Berkeley  $GW$  method and useful discussions on exciton physics in 2D materials. J.Z. appreciates Professor A.S. Rodin for the helpful discussions. This work is supported by the National Basic Research Program of China (973 Program No. 2019YFA0308402) and the National Natural Science Foundation of China under Grant No. 51972217.

#### APPENDIX A: CONVERGENCE OF $G_0W_0$ -BSE CALCULATIONS OF BLUE PHOSPHORENE

In Fig. 19, we show the convergence of quasiparticle band energies in blue phosphorene with respect to the scale of the  $k$  grid (coarse grid), the dielectric cutoff, and the number of bands. In Fig. 20, we show the convergence of the exciton energy in blue phosphorene with respect to the scale of the  $k$  grid (fine grid).

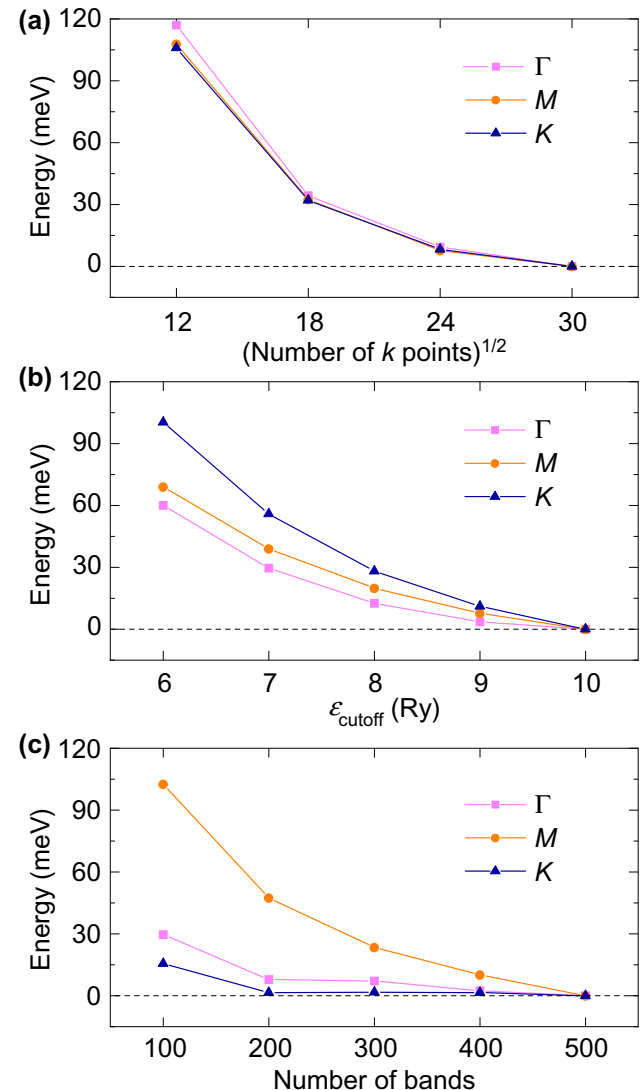


FIG. 19. The convergence of the quasiparticle ( $G_0W_0$ ) band gap at three high-symmetry  $k$  points with respect to (a) the scale of the coarse  $k$  grid, (b) the dielectric cutoff energy ( $\epsilon_{\text{cutoff}}$ ), and (c) the number of bands. In (a), we use a  $\epsilon_{\text{cutoff}}$  of 10 Ry and 500 bands; in (b), we use a  $k$  grid of  $30 \times 30 \times 1$  and 500 bands; and in (c), we use a  $\epsilon_{\text{cutoff}}$  of 10 Ry and a  $k$  grid of  $30 \times 30 \times 1$ . With the above considerations, we use a  $30 \times 30 \times 1$   $k$  grid, a  $\epsilon_{\text{cutoff}}$  of 10 Ry, and 500 bands for our  $G_0W_0$  calculations.

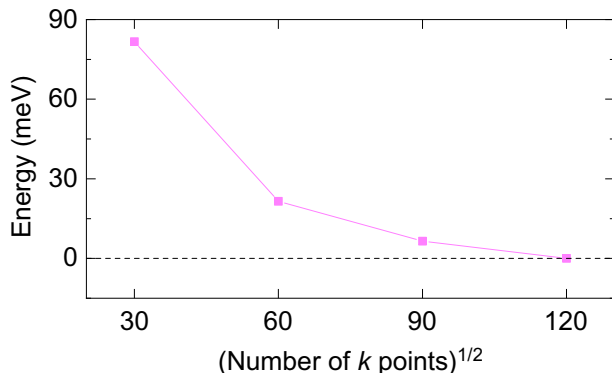


FIG. 20. The convergence of the energy of the 1s exciton state in BSE calculations with respect to the scale of the fine  $k$  grids: including  $30 \times 30 \times 1$ ,  $60 \times 60 \times 1$ ,  $90 \times 90 \times 1$ , and  $120 \times 120 \times 1$ . With the above considerations, we use a  $120 \times 120 \times 1$   $k$  grid in our BSE calculations.

## APPENDIX B: MAXIMUM LOCALIZED WANNIER ORBITALS IN BLUE PHOSPHORENE

Using Wannier90 [59], the orbital-decomposed band structure (PBE level) and the total density of states (DOS) are shown in Fig. 21.

## APPENDIX C: STRAIN DEPENDENCE OF BAND GAP IN BLUE PHOSPHORENE

In Fig. 22, we show the strain dependence of the band gap of blue phosphorene within the PBE level.

## APPENDIX D: QUASIPARTICLE ELECTRONIC STRUCTURE AND OPTICAL ABSORPTION SPECTRUM OF THREE 2D INDIRECT-BAND-GAP SEMICONDUCTORS MONOCHALCOGENIDES

In Figs. 23–25, we show the electronic band structure and the optical absorption spectrum (within the  $G_0W_0$ -BSE framework) for the 2D materials GaS, GaSe, and InSe,

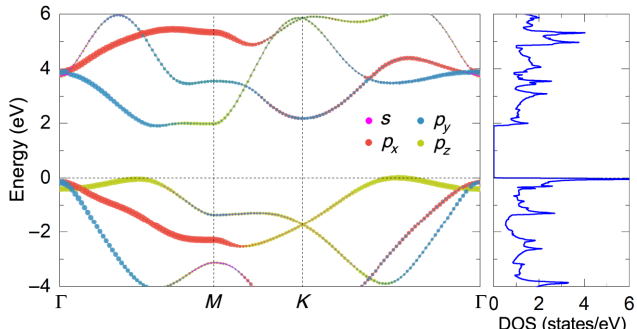


FIG. 21. The left-hand panel shows the orbital-decomposed band structure (DFT-PBE level) of blue phosphorene from maximum localized Wannier orbitals using Wannier90 [59]. The total DOS is shown in the right-hand panel.

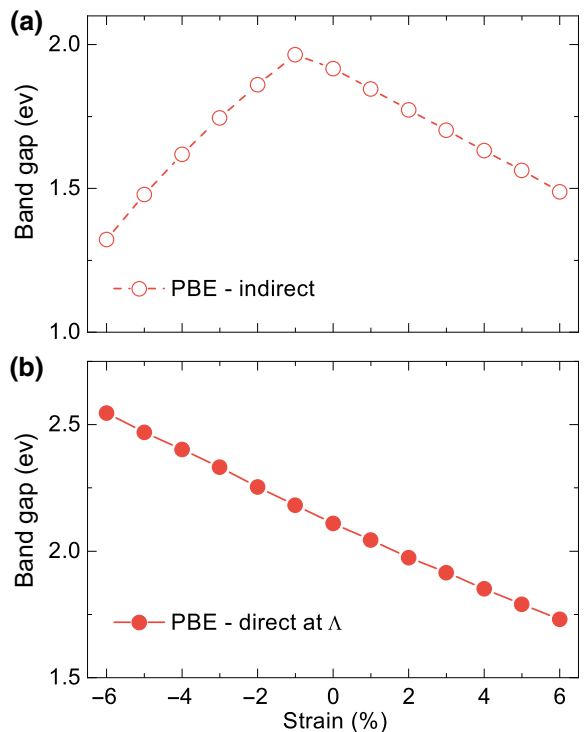


FIG. 22. The evolution of the band gaps (PBE level) in blue phosphorene with biaxial strain: (a) indirect band gap; (b) direct band gap at point  $\Lambda$ .

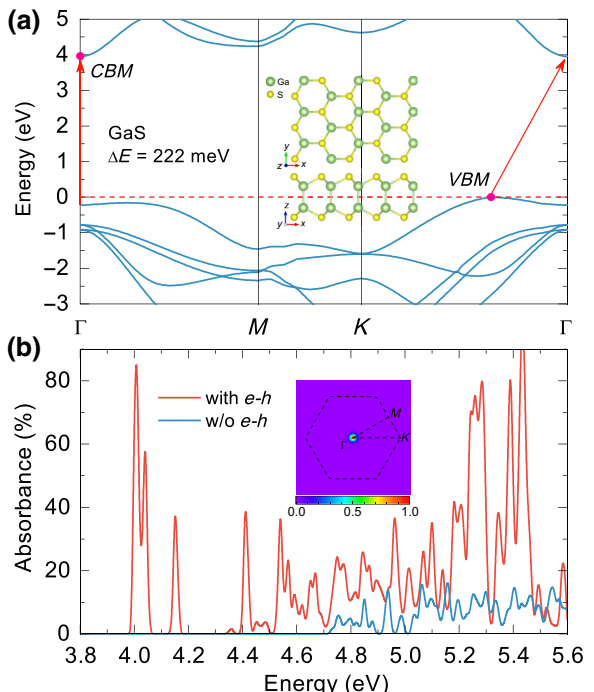


FIG. 23. The quasiparticle electronic band structure (a) and the optical absorption spectrum (b) of 2D GaS from  $G_0W_0$ -BSE calculations. The insets show the crystal structure and the  $k$ -space plot of the exciton for the first absorption peak. Here, the energy difference between the direct and indirect transitions is 222 meV.

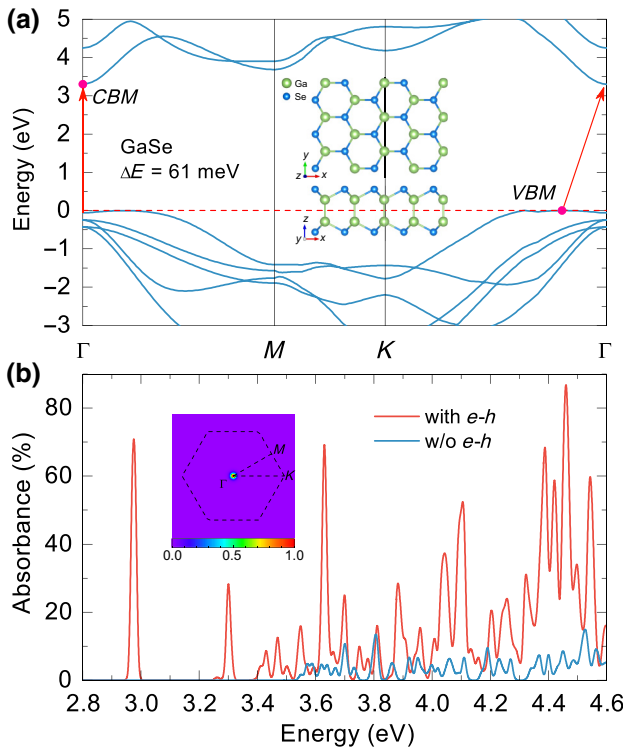


FIG. 24. The quasiparticle electronic band structure (a) and the optical absorption spectrum (b) of 2D GaSe from *GW*-BSE calculations. The insets show the crystal structure and the  $k$ -space plot of the exciton for the first absorption peak. Here, the energy difference between the direct and indirect transitions is 61 meV.

respectively. Photoluminescence has been found in these 2D materials [22,23]. Clearly, these three 2D materials are indirect-band-gap semiconductors. The energy differences between direct and indirect transitions are 222, 61, and 34 meV, respectively. Similar to blue phosphorene, the first optical absorption shows a strong amplitude in these 2D materials. With the scenario of the Maxwell-Boltzmann distribution, the recombination rate between the direct and indirect channels, i.e., the luminescence effect, is proportional to  $e^{-\Delta E/k_B T}$ , where  $\Delta E$  is the energy difference between the direct and indirect channels and  $T$  is the temperature. For GaS, GaSe, and InSe, the ratios are 0.0002, 0.1, and 0.27, respectively. For blue phosphorene, the energy difference between the direct and indirect band gaps is around 48 meV for the pristine system and the value will decrease to less than 17 meV when sufficient tensile strain is applied. Here, the quasiparticle band structures and optical properties of GaS, GaSe, and InSe are calculated using the QUANTUM ESPRESSO and BerkeleyGW software. A slab model is used, with a vacuum layer of 15 Å along the out-of-plane direction. We use the norm-conserving PBE pseudopotentials with a plane-wave cutoff of 80 Ry. For the *GW* part, we use a coarse  $k$  grid of  $24 \times 24 \times 1$  and 931 empty bands, with the highest

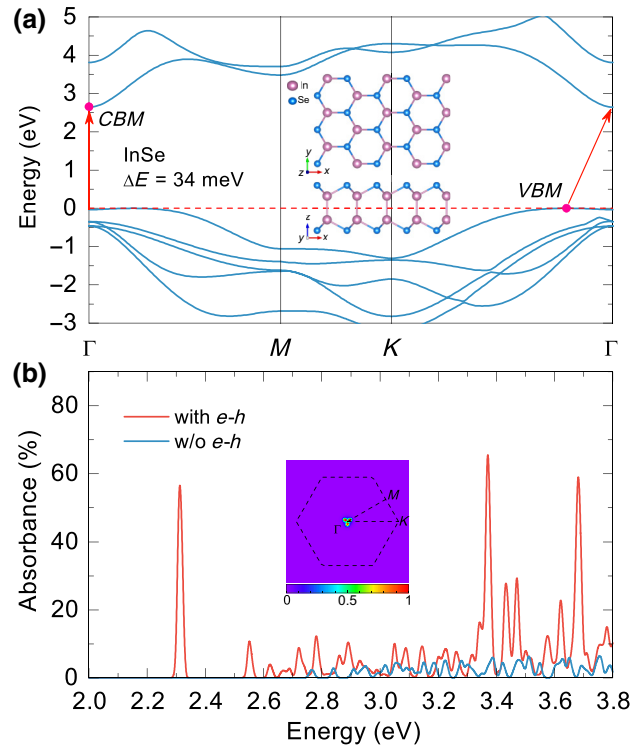


FIG. 25. The quasiparticle electronic band structure (a) and the optical absorption spectrum (b) of 2D InSe from *GW*-BSE calculations. The insets show the crystal structure and the  $k$ -space plot of the exciton for the first absorption peak. Here, the energy difference between the direct and indirect transitions is 34 meV.

unoccupied state at 9.4 Ry (19 occupied bands with the lowest occupied state at -1.1 Ry) and a dielectric cutoff of 15 Ry. For the BSE part, a fine  $k$  grid of  $72 \times 72 \times 1$  is used. Gaussian smearing with a broadening constant of 5 meV is used in the optical absorption spectrum. The number of bands for optical transitions is five for both valence bands and three for conduction bands, which is sufficient to cover the span of the visible light.

- [1] A. H. Castro Neto, F. Guinea, N. M. R. Peres, K. S. Novoselov, and A. K. Geim, The electronic properties of graphene, *Rev. Mod. Phys.* **81**, 109 (2009).
- [2] D. N. Basov, M. M. Fogler, A. Lanzara, F. Wang, and Y. Zhang, Colloquium: Graphene spectroscopy, *Rev. Mod. Phys.* **86**, 959 (2014).
- [3] K. S. Novoselov, D. Jiang, F. Schedin, T. J. Booth, V. V. Khotkevich, S. V. Morozov, and A. K. Geim, Two-dimensional atomic crystals, *Proc. Natl. Acad. Sci. U.S.A.* **102**, 10451 (2005).
- [4] P. Ajayan, P. Kim, and K. Banerjee, Van der Waals materials, *Phys. Today* **69**, 38 (2016).
- [5] Q. H. Wang, K. Kalantar-Zadeh, A. Kis, J. N. Coleman, and M. S. Strano, Electronics and optoelectronics

- of two-dimensional transition metal dichalcogenides, *Nat. Nanotechnol.* **7**, 699 (2012).
- [6] G. Fiori, F. Bonaccorso, G. Iannaccone, T. Palacios, D. Neumaier, A. Seabaugh, S. K. Banerjee, and L. Colombo, Electronics based on two-dimensional materials, *Nat. Nanotechnol.* **9**, 768 (2014).
- [7] F. H. L. Koppens, T. Mueller, P. Avouris, A. C. Ferrari, M. S. Vitiello, and M. Polini, Photodetectors based on graphene, other two-dimensional materials and hybrid systems, *Nat. Nanotechnol.* **9**, 780 (2014).
- [8] F. Xia, H. Wang, D. Xiao, M. Dubey, and A. Ramasubramaniam, Two-dimensional material nanophotonics, *Nat. Photonics* **8**, 899 (2014).
- [9] K. F. Mak and J. Shan, Photonics and optoelectronics of 2D semiconductor transition metal dichalcogenides, *Nat. Photonics* **10**, 216 (2016).
- [10] Z. Sun, A. Martinez, and F. Wang, Optical modulators with 2D layered materials, *Nat. Photonics* **10**, 227 (2016).
- [11] AM 1.5 G solar spectrum from <http://rredc.nrel.gov/solar/spectra/am1.5>.
- [12] G. Schusteritsch, M. Uhrin, and C. J. Pickard, Single-layered Hittorf's phosphorus: A wide-bandgap high mobility 2D material, *Nano Lett.* **16**, 2975 (2016).
- [13] L. Zhang, H. Huang, B. Zhang, M. Gu, D. Zhao, X. Zhao, L. Li, J. Zhou, K. Wu, Y. Cheng, and J. Zhang, Structure and properties of violet phosphorus and its phosphorene exfoliation, *Angew. Chem. Int. Ed.* **59**, 1074 (2020).
- [14] J. Zhou, T. Y. Cai, and S. Ju, Anisotropic exciton excitations and optical properties of Hittorf's phosphorene, *Phys. Rev. Res.* **2**, 033288 (2020).
- [15] Z. Zhu and D. Tománek, Semiconducting Layered Blue Phosphorus: A Computational Study, *Phys. Rev. Lett.* **112**, 176802 (2014).
- [16] C. E. P. Villegas, A. S. Rodin, A. Carvalho, and A. R. Rocha, Two-dimensional exciton properties in monolayer semiconducting phosphorus allotropes, *Phys. Chem. Chem. Phys.* **18**, 27829 (2016).
- [17] W. H. Han, S. Kim, I. Lee, and K. J. Chang, Prediction of green phosphorus with tunable direct band gap and high mobility, *J. Phys. Chem. Lett.* **8**, 4627 (2017).
- [18] H. Shu, Y. Wang, and M. Sun, Enhancing electronic and optical properties of monolayer MoSe<sub>2</sub> via a MoSe<sub>2</sub>/blue phosphorene heterobilayer, *Phys. Chem. Chem. Phys.* **21**, 15760 (2019).
- [19] F. Iyikanat, E. Torun, R. T. Senger, and H. Sahin, Stacking-dependent excitonic properties of bilayer blue phosphorene, *Phys. Rev. B* **100**, 125423 (2019).
- [20] M. R. Fiorentin, G. Cicero, and M. Palummo, Spatially indirect excitons in black and blue phosphorene double layers, *Phys. Rev. Mater.* **4**, 074009 (2020).
- [21] T. Cao, Z. Li, and S. G. Louie, Tunable Magnetism and Half-Metallicity in Hole-Doped Monolayer GaSe, *Phys. Rev. Lett.* **114**, 236602 (2015).
- [22] C. S. Jung, F. Shojaei, K. Park, J. Y. Oh, H. S. Im, D. M. Jang, J. Park, and H. S. Kang, Red-to-ultraviolet emission tuning of two-dimensional gallium sulfide/selenide, *ACS Nano* **9**, 9585 (2015).
- [23] D. A. Bandurin, A. V. Tyurnina, G. L. Yu, A. Mishchenko, V. Zólyomi, S. V. Morozov, R. K. Kumar, R. V. Gorbachev, Z. R. Kudrynskyi, S. Pezzini, Z. D. Kovalyuk, U. Zeitler, K. S. Novoselov, A. Patanè, L. Eaves, I. V. Grigorieva, V. I. Fal'ko, A. K. Geim, and Y. Cao, High electron mobility, quantum Hall effect and anomalous optical response in atomically thin InSe, *Nat. Nanotechnol.* **12**, 223 (2017).
- [24] Y. Li, T. Wang, M. Wu, T. Cao, Y. Chen, R. Sankar, R. K. Ulaganathan, F. Chou, C. Wetzel, C. Y. Xu, S. G. Louie, and S. F. Shi, Ultrasensitive tunability of the direct bandgap of 2D InSe flakes via strain engineering, *2D Mater.* **5**, 021002 (2018).
- [25] C. H. Park, C. D. Spataru, and S. G. Louie, Excitons and Many-Electron Effects in the Optical Response of Single-Walled Boron Nitride Nanotubes, *Phys. Rev. Lett.* **96**, 126105 (2006).
- [26] C. H. Park and S. G. Louie, Energy gaps and Stark effect in boron nitride nanoribbons, *Nano Lett.* **8**, 2200 (2008).
- [27] L. Ci, L. Song, C. Jin, D. Jariwala, D. Wu, Y. Li, A. Srivastava, Z. F. Wang, K. Storr, L. Balicas, F. Liu, and P. M. Ajayan, Atomic layers of hybridized boron nitride and graphene domains, *Nat. Mater.* **9**, 430 (2010).
- [28] F. A. Ponce and D. P. Bour, Nitride-based semiconductors for blue and green light-emitting devices, *Nature* **386**, 351 (1997).
- [29] J. L. Zhang, S. Zhao, C. Han, Z. Wang, S. Zhong, S. Sun, R. Guo, X. Zhou, C. D. Gu, K. D. Yuan, Z. Li, and W. Chen, Epitaxial growth of single layer blue phosphorus: A new phase of two-dimensional phosphorus, *Nano Lett.* **16**, 4903 (2016).
- [30] C. Gu, S. Zhao, J. L. Zhang, S. Sun, K. Yuan, Z. Hu, C. Han, Z. Ma, L. Wang, F. Huo, W. Huang, Z. Li, and W. Chen, Growth of quasi-free-standing single-layer blue phosphorus on tellurium monolayer functionalized Au (111), *ACS Nano* **11**, 4943 (2017).
- [31] J. P. Xu, J. Q. Zhang, H. Tian, H. Xu, W. Ho, and M. Xie, One-dimensional phosphorus chain and two-dimensional blue phosphorene grown on Au (111) by molecular-beam epitaxy, *Phys. Rev. Mater.* **1**, 061002(R) (2017).
- [32] E. Golias, M. Krivenkov, A. Varykhalov, J. Sánchez-Barriga, and O. Rader, Band renormalization of blue phosphorus on Au (111), *Nano Lett.* **18**, 6672 (2018).
- [33] J. L. Zhang, S. Zhao, M. Telychko, S. Sun, X. Lian, J. Su, A. Tadich, D. Qi, J. Zhuang, Y. Zheng, Z. Ma, C. Gu, Z. Hu, Y. Du, J. Lu, Z. Li, and W. Chen, Reversible oxidation of blue phosphorus monolayer on Au (111), *Nano Lett.* **19**, 5340 (2019).
- [34] J. L. Zhang *et al.*, Synthesis of monolayer blue phosphorus enabled by silicon intercalation, *ACS Nano* **14**, 3687 (2020).
- [35] L. V. Keldysh, Coulomb interaction in thin semiconductor and semimetal films, *JETP Lett.* **29**, 658 (1979).
- [36] P. Cudazzo, I. V. Tokatly, and A. Rubio, Dielectric screening in two-dimensional insulators: Implications for excitonic and impurity states in graphane, *Phys. Rev. B* **84**, 085406 (2011).
- [37] T. C. Berkelbach, M. S. Hybertsen, and D. R. Reichman, Theory of neutral and charged excitons in monolayer transition metal dichalcogenides, *Phys. Rev. B* **88**, 045318 (2013).
- [38] D. Y. Qiu, F. H. da Jornada, and S. G. Louie, Optical Spectrum of MoS<sub>2</sub>: Many-Body Effects and Diversity of

- Exciton States, *Phys. Rev. Lett.* **111**, 216805 (2013).*ibid* **115**, 119901 (2015)
- [39] F. Hüser, T. Olsen, and K. S. Thygesen, How dielectric screening in two-dimensional crystals affects the convergence of excited-state calculations: Monolayer MoS<sub>2</sub>, *Phys. Rev. B* **88**, 245309 (2013).
- [40] A. S. Rodin, A. Carvalho, and A. H. Castro Neto, Excitons in anisotropic two-dimensional semiconducting crystals, *Phys. Rev. B* **90**, 075429 (2014).
- [41] R. Soklaski, Y. Liang, and L. Yang, Temperature effect on optical spectra of monolayer molybdenum disulfide, *Appl. Phys. Lett.* **104**, 193110 (2014).
- [42] V. Tran, R. Soklaski, Y. Liang, and L. Yang, Layer-controlled band gap and anisotropic excitons in few-layer black phosphorus, *Phys. Rev. B* **89**, 235319 (2014).
- [43] V. Tran, R. Fei, and L. Yang, Quasiparticle energies, excitons, and optical spectra of few-layer black phosphorus, *2D Mater.* **2**, 044014 (2015).
- [44] J. Choi, P. Cui, H. Lan, and Z. Zhang, Linear Scaling of the Exciton Binding Energy versus the Band Gap of Two-Dimensional Materials, *Phys. Rev. Lett.* **115**, 066403 (2015).
- [45] G. Shi and E. Kioupakis, Anisotropic spin transport and strong visible-light absorbance in few-layer SnSe and GeSe, *Nano Lett.* **15**, 6926 (2015).
- [46] T. Olsen, S. Latini, F. Rasmussen, and K. S. Thygesen, Simple Screened Hydrogen Model of Excitons in Two-Dimensional Materials, *Phys. Rev. Lett.* **116**, 056401 (2016).
- [47] D. Y. Qiu, F. H. da Jornada, and S. G. Louie, Screening and many-body effects in two-dimensional crystals: Monolayer MoS<sub>2</sub>, *Phys. Rev. B* **93**, 235435 (2016).
- [48] Z. Jiang, Z. Liu, Y. Li, and W. Duan, Scaling Universality between Band Gap and Exciton Binding Energy of Two-Dimensional Semiconductors, *Phys. Rev. Lett.* **118**, 266401 (2017).
- [49] W. Song and L. Yang, Quasiparticle band gaps and optical spectra of strained monolayer transition-metal dichalcogenides, *Phys. Rev. B* **96**, 235441 (2017).
- [50] D. Y. Qiu, F. H. da Jornada, and S. G. Louie, Environmental screening effects in 2D materials: Renormalization of the bandgap, electronic structure, and optical spectra of few-layer black phosphorus, *Nano Lett.* **17**, 4706 (2017).
- [51] N. Sanders, D. Bayerl, G. Shi, K. A. Mengle, and E. Kioupakis, Electronic and optical properties of two-dimensional GaN from first-principles, *Nano Lett.* **17**, 7345 (2017).
- [52] P. Giannozzi, S. Baroni, N. Bonini, M. Calandra, R. Car, C. Cavazzoni, D. Ceresoli, G. L. Chiarotti, M. Cococcioni, I. Dabo, A. D. Corso, S. de Gironcoli, S. Fabris, G. Fratesi, R. Gebauer, U. Gerstmann, C. Gougaussis, A. Kokalj, M. Lazzeri, L. Martin-Samos, N. Marzari, F. Mauri, R. Mazzarello, S. Paolini, A. Pasquarello, L. Paulatto, C. Sbraccia, S. Scandolo, G. Scalauzero, A. P. Seitsonen, A. Smogunov, P. Umari, and R. M. Wentzcovitch, QUANTUM ESPRESSO: A modular and open-source software project for quantum simulations of materials, *J. Phys.: Condens. Matter* **21**, 395502 (2009).
- [53] M. S. Hybertsen and S. G. Louie, Electron correlation in semiconductors and insulators: Band gaps and quasiparticle energies, *Phys. Rev. B* **34**, 5390 (1986).
- [54] M. Rohlfing and S. G. Louie, Electron-hole excitations and optical spectra from first principles, *Phys. Rev. B* **62**, 4927 (2000).
- [55] J. Deslippe, G. Samzonidze, D. A. Strubbe, M. Jain, M. L. Cohen, and S. G. Louie, BerkeleyGW: A massively parallel computer package for the calculation of the quasiparticle and optical properties of materials and nanostructures, *Comput. Phys. Commun.* **183**, 1269 (2012).
- [56] J. P. Perdew, K. Burke, and M. Ernzerhof, Generalized Gradient Approximation Made Simple, *Phys. Rev. Lett.* **77**, 3865 (1996).
- [57] D. R. Hamann, Optimized norm-conserving Vanderbilt pseudopotentials, *Phys. Rev. B* **88**, 085117 (2013).
- [58] B. C. Shih, Y. Xue, P. Zhang, M. L. Cohen, and S. G. Louie, Quasiparticle Band Gap of ZnO: High Accuracy from the Conventional  $G^0W^0$  Approach, *Phys. Rev. Lett.* **105**, 146401 (2010).
- [59] G. Pizzi, V. Vitale, R. Arita, S. Blügel, F. Freimuth, G. Géranton, M. Gibertini, D. Gresch, C. Johnson, T. Koretsune, J. Ibañez-Azpiroz, H. Lee, J. Lihm, D. Marchand, A. Marrazzo, Y. Mokrousov, J. I. Mustafa, Y. Nohara, Y. Nomura, L. Paulatto, S. Poncé, T. Ponweiser, J. Qiao, F. Thöle, S. S. Tsirkin, M. Wierzbowska, N. Marzari, D. Vanderbilt, I. Souza, A. A. Mostofi, and J. R. Yates, Wannier90 as a community code: New features and applications, *J. Phys.: Condens. Matter* **32**, 165902 (2020).
- [60] C. D. Spataru, S. Ismail-Beigi, R. B. Capaz, and S. G. Louie, Theory and *ab initio* Calculation of Radiative Lifetime of Excitons in Semiconducting Carbon Nanotubes, *Phys. Rev. Lett.* **95**, 247402 (2005).
- [61] M. Palummo, M. Bernardi, and J. C. Grossman, Exciton radiative lifetimes in two-dimensional transition metal dichalcogenides, *Nano Lett.* **15**, 2794 (2015).
- [62] T. Langer, A. Chernikov, D. Kalincev, M. Gerhard, H. Bremer, U. Rossow, M. Koch, and A. Hangleiter, Room temperature excitonic recombination in GaInN/GaN quantum wells, *Appl. Phys. Lett.* **103**, 202106 (2013).
- [63] Y. Chen and S. Y. Quek, Tunable bright interlayer excitons in few-layer black phosphorus based van der Waals heterostructures, *2D Mater.* **5**, 045031 (2018).
- [64] T. Korn, S. Heydrich, M. Hirmer, J. Schmutzler, and C. Schüller, Low-temperature photocarrier dynamics in monolayer MoS<sub>2</sub>, *Appl. Phys. Lett.* **99**, 102109 (2011).
- [65] D. Lagarde, L. Bouet, X. Marie, C. R. Zhu, B. L. Liu, T. Amand, P. H. Tan, and B. Urbaszek, Carrier and Polarization Dynamics in Monolayer MoS<sub>2</sub>, *Phys. Rev. Lett.* **112**, 047401 (2014).
- [66] H. Shi, R. Yan, S. Bertolazzi, J. Brivio, B. Gao, A. Kis, D. Jena, H. G. Xing, and L. Huang, Exciton dynamics in suspended monolayer and few-layer MoS<sub>2</sub> 2D crystals, *ACS Nano* **7**, 1072 (2013).
- [67] C. Robert, D. Lagarde, F. Cadiz, G. Wang, B. Lassagne, T. Amand, A. Balocchi, P. Renucci, S. Tongay, B. Urbaszek, and X. Marie, Exciton radiative lifetime in transition metal dichalcogenide monolayers, *Phys. Rev. B* **93**, 205423 (2016).
- [68] N. Kumar, Q. Cui, F. Ceballos, D. He, Y. Wang, and H. Zhao, Exciton-exciton annihilation in MoSe<sub>2</sub> monolayers, *Phys. Rev. B* **89**, 125427 (2014).
- [69] G. Wang, L. Bouet, D. Lagarde, M. Vidal, A. Balocchi, T. Amand, X. Marie, and B. Urbaszek, Valley dynamics

- probed through charged and neutral exciton emission in monolayer WSe<sub>2</sub>, *Phys. Rev. B* **90**, 075413 (2014).
- [70] S. Mouri, Y. Miyauchi, M. Toh, W. Zhao, G. Eda, and K. Matsuda, Nonlinear photoluminescence in atomically thin layered WSe<sub>2</sub> arising from diffusion-assisted exciton-exciton annihilation, *Phys. Rev. B* **90**, 155449 (2014).
- [71] A. Pospischil, M. M. Furchi, and T. Mueller, Solar-energy conversion and light emission in an atomic monolayer *p-n* diode, *Nat. Nanotechnol.* **9**, 257 (2014).
- [72] B. W. H. Baugher, H. O. H. Churchill, Y. Yang, and P. Jarillo-Herrero, Optoelectronic devices based on electrically tunable *p-n* diodes in a monolayer dichalcogenide, *Nat. Nanotechnol.* **9**, 262 (2014).
- [73] J. S. Ross, P. Klement, A. M. Jones, N. J. Ghimire, J. Yan, D. G. Mandrus, T. Taniguchi, K. Watanabe, K. Kitamura, W. Yao, D. H. Cobden, and X. Xu, Electrically tunable excitonic light-emitting diodes based on monolayer WSe<sub>2</sub> *p-n* junctions, *Nat. Nanotechnol.* **9**, 268 (2014).
- [74] R. Z. Bachrach, W. B. Joyce, and R. W. Dixon, Optical-coupling efficiency of GaP:N green-light-emitting diodes, *J. Appl. Phys.* **44**, 5458 (1973).
- [75] G. A. Herrmannsfeldt and Y. C. Chang, High-pressure studies of luminescence from GaP and GaP:N diodes, *Phys. Rev. B* **34**, 5373 (1986).
- [76] L. Bellaiche, S. H. Wei, and A. Zunger, Composition dependence of interband transition intensities in GaPN, GaAsN, and GaPAs alloys, *Phys. Rev. B* **56**, 10233 (1997).
- [77] H. P. Xin, C. W. Tu, Y. Zhang, and A. Mascarenhas, Effects of nitrogen on the band structure of GaN<sub>x</sub>P<sub>1-x</sub> alloys, *Appl. Phys. Lett.* **76**, 1267 (2000).
- [78] W. Shan, W. Walukiewicz, K. M. Yu, J. Wu, J. W. Ager, E. E. Haller, H. P. Xin, and C. W. Tu, Nature of the fundamental band gap in GaN<sub>x</sub>P<sub>1-x</sub> alloys, *Appl. Phys. Lett.* **76**, 3251 (2000).
- [79] I. A. Buyanova, G. Y. Rudko, W. M. Chen, H. P. Xin, and C. W. Tu, Radiative recombination mechanism in GaN<sub>x</sub>P<sub>1-x</sub> alloys, *Appl. Phys. Lett.* **80**, 1740 (2002).
- [80] I. A. Buyanova, G. Pozina, J. P. Bergman, W. M. Chen, and C. W. Tu, Time-resolved studies of photoluminescence in GaN<sub>x</sub>P<sub>1-x</sub> alloys: Evidence for indirect-direct band gap crossover, *Appl. Phys. Lett.* **81**, 52 (2002).
- [81] J. Chamings, S. Ahmed, S. J. Sweeney, V. A. Odnoblyudov, and C. W. Tu, Physical properties and efficiency of GaNP light emitting diodes, *Appl. Phys. Lett.* **92**, 021101 (2008).
- [82] J. Feng, X. Qian, C. Huang, and J. Li, Strain-engineered artificial atom as a broad-spectrum solar energy funnel, *Nat. Photonics* **6**, 866 (2012).
- [83] P. San-Jose, V. Parente, F. Guinea, R. Roldán, and E. Prada, Inverse Funnel Effect of Excitons in Strained Black Phosphorus, *Phys. Rev. X* **6**, 031046 (2016).
- [84] A. Föppl, *Vorlesungen über technische Mechanik* (B. G. Teubner, Leipzig, 1907, Vol.1, 132).
- [85] H. Hencky, Über den Spannungszustand in kreisrunden Platten, *Z. Math. Phys.* **63**, 311 (1915).
- [86] O. N. Scott, M. R. Begley, U. Komaragini, and T. J. Mackin, Indentation of freestanding circular elastomer films using spherical indenters, *Acta Mater.* **52**, 4877 (2004).
- [87] C. Jin, A. Davoodabadi, J. Li, Y. Wang, and T. Singler, Spherical indentation of a freestanding circular membrane revisited: Analytical solutions and experiments, *J. Mech. Phys. Solids* **100**, 85 (2017).
- [88] A. C. De Palma, G. Cossio, K. Jones, J. Quan, X. Li, and E. T. Yu, Strain-dependent luminescence and piezoelectricity in monolayer transition metal dichalcogenides, *J. Vac. Sci. Technol. B* **38**, 042205 (2020).